J. Magn. Soc. Jpn., **40**, 137-147 (2016)

<Paper>

Influence of Composition on the Crystal Structure of Fe-Ni Alloy Epitaxial Thin Film Deposited on Cr(211) Underlayer

Shigeyuki Minakawa[1], Mitsuru Ohtake[1], Masaaki Futamoto[1], Fumiyoshi Kirino[2], and Nobuyuki Inaba[3]

[1]Faculty of Science and Engineering, Chuo University, *1-13-27 Kasuga, Bunkyo-ku, Tokyo 112-8551, Japan*

[2]Graduate School of Fine Arts, Tokyo University of the Arts, *12-8 Ueno-koen, Taito-ku, Tokyo 110-8714, Japan*

[3]Faculty of Engineering, Yamagata University, *4-3-16 Jyonan, Yonezawa, Yamagata 992-8510, Japan*

$Fe_{100-x}Ni_x$ (x = 0–100 at. %) alloy epitaxial films of 10 nm thickness are prepared on Cr(211) underlayers at room temperature by using a radio-frequency magnetron sputtering system. The film growth behavior and the crystallographic properties are investigated by *in-situ* reflection high-energy electron diffraction and pole-figure X-ray diffraction. bcc(211) crystal epitaxially nucleates on the underlayer for the $Fe_{100-x}Ni_x$ films with x = 0–70 at. %. The bcc structure is stabilized up to 10 nm thickness for the compositional range of x = 0–50 at. %, whereas the $Fe_{40}Ni_{60}$ and the $Fe_{30}Ni_{70}$ crystals with bcc structure (x = 60–70 at. %) start to transform into fcc structure with increasing the thickness beyond 2 and 5 nm, respectively. The bcc-fcc phase transformation occurs through atomic displacements parallel to bcc(110) and bcc(101) close-packed planes which are 60° canted from the perpendicular direction. The crystallographic orientation relationship is similar to the Kurdjumov-Sachs relationship. When the x value is increased beyond 80 at. %, metastable hcp($1\bar{1}00$) crystal coexists with bcc(211) crystal. The volume ratio of hcp to bcc crystal increases as the x value increases from 80 to 100 at. %. With increasing the thickness, the hcp crystal also starts to transform into fcc structure through atomic displacement parallel to hcp(0001) close-packed plane, which is similar to the case of bulk phase transformation in the Shoji-Nishiyama relationship.

Key words: Fe-Ni alloy thin film, epitaxial growth, bcc, fcc, hcp, crystal structure, phase transformation

1. Introduction

Thin films of 3*d* ferromagnetic transition metals or their alloys have been widely studied for applications such as magnetic sensors, magnetic recording media, etc. Recently, magnetic films with metastable structures have attracted much attention, since new possibilities are recognized. For example, magnetic tunnel junction elements prepared by employing Co films with metastable bcc structure have been reported to show high tunnel magnetoresistance ratios[1–3]. The magnetic and electronic properties are greatly affected by their crystal structures. It is thus important to understand the formation conditions of films with metastable structures.

Fe, Ni, and Fe-Ni alloy materials are typical soft magnetic materials. In the bulk Fe-Ni binary alloy system[4], there are bcc ($A2$) and fcc ($A1$, $L1_2$) phases. On the contrary, metastable hcp ($A3$) phase has been recognized for Ni and $Fe_{20}Ni_{80}$ (at. %) films epitaxially grown on Cr[5–9], V[9], Au[10,11], MgO[12,13], and Ru[14] materials. Epitaxial thin film growth technique has a possibility in forming films with metastable structures. In our previous studies[6–8], Ni and $Fe_{20}Ni_{80}$ films of 40 nm thickness were sputter-deposited on Cr(211) underlayers at room temperature (RT). The crystallographic property during film formation was investigated by *in-situ* reflection high-energy electron diffraction (RHEED). hcp-Ni and hcp-$Fe_{20}Ni_{80}$ crystals of ($1\bar{1}00$) orientation nucleated on the underlayers. However with increasing the thickness, the hcp crystal started to transform into fcc structure and the volume ratio of hcp to transformed fcc crystal increased for both films.

The crystallographic properties are considered to be influenced by the film composition. However, the compositional dependence has not been made clear, yet. In the present study, $Fe_{100-x}Ni_x$ films are prepared on Cr(211) underlayers by varying the composition in the full range, x = 0–100 at. %. The growth behavior and the detailed structure property are investigated by *in-situ* RHEED and pole-figure X-ray diffraction (XRD).

2. Experimental Procedure

Thin films were deposited on polished MgO(110) single-crystal substrates by using a radio-frequency (RF) magnetron sputtering system with the base pressure lower than 4×10^{-7} Pa. Fe, Ni, and Cr targets of 3 inch diameter were used and the respective RF powers were fixed at 50, 58, and 40 W. The distance between target and substrate and the Ar gas pressure were kept constant at 150 mm and 0.67 Pa, respectively. Under the conditions, the deposition rate was 0.02 nm/s for all the materials.

MgO substrates were heated at 600 °C for 1 hour before film formation to obtain clean surfaces. 10-nm-thick Cr underlayers were deposited on the substrates at 300 °C. The substrate temperature was used to promote epitaxial growth of Cr underlayer on

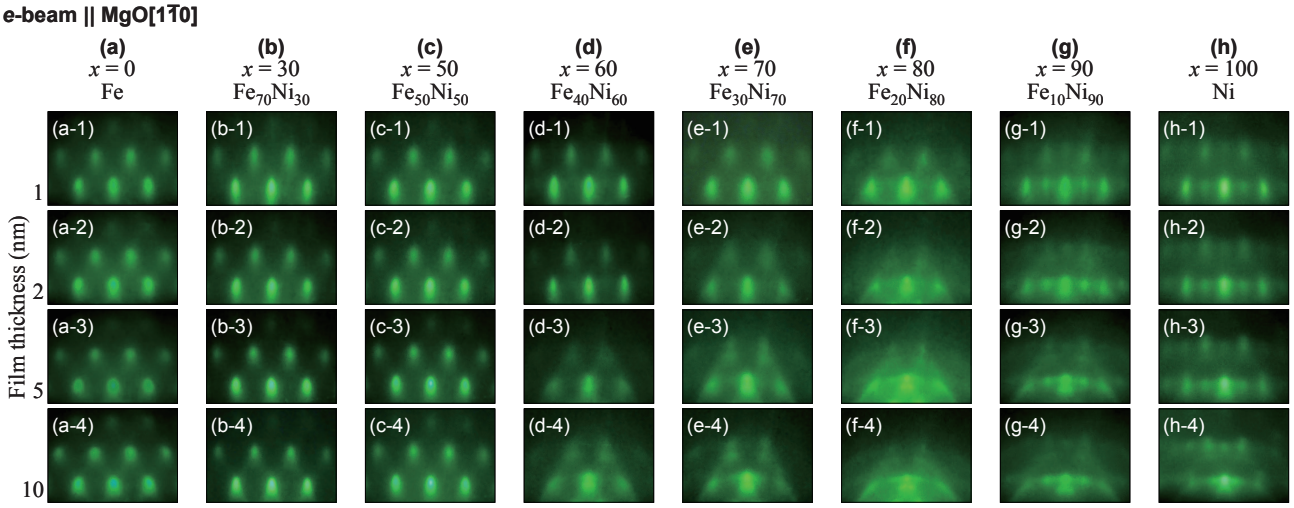

Fig. 1 RHEED patterns observed during formation of (a) Fe, (b) $Fe_{70}Ni_{30}$, (c) $Fe_{50}Ni_{50}$, (d) $Fe_{40}Ni_{60}$, (e) $Fe_{30}Ni_{70}$, (f) $Fe_{20}Ni_{80}$, (g) $Fe_{10}Ni_{90}$, and (h) Ni films on Cr(211) underlayers. The film thicknesses are (a-1)–(h-1) 1 nm, (a-2)–(h-2) 2 nm, (a-3)–(h-3) 5 nm, and (a-4)–(h-4) 10 nm. The incident electron beam is parallel to MgO[1$\bar{1}$0].

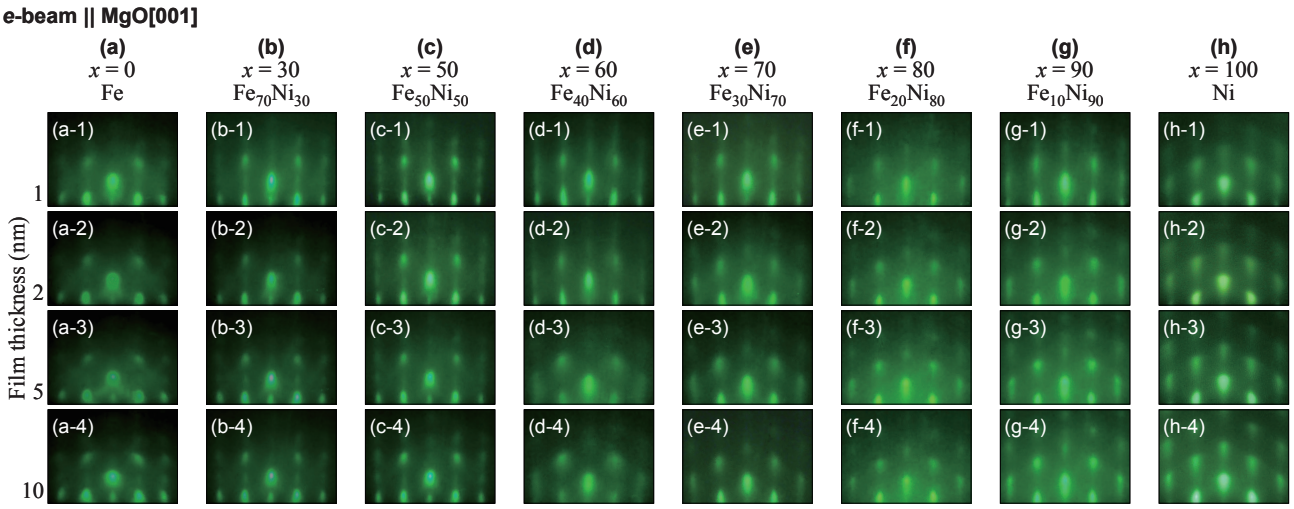

Fig. 2 RHEED patterns observed during formation of (a) Fe, (b) $Fe_{70}Ni_{30}$, (c) $Fe_{50}Ni_{50}$, (d) $Fe_{40}Ni_{60}$, (e) $Fe_{30}Ni_{70}$, (f) $Fe_{20}Ni_{80}$, (g) $Fe_{10}Ni_{90}$, and (h) Ni films on Cr(211) underlayers. The film thicknesses are (a-1)–(h-1) 1 nn, (a-2)–(h-2) 2 nm, (a-3)–(h-3) 5 nm, and (a-4)–(h-4) 10 nm. The incident electron beam is parallel to MgO[001].

MgO(110) substrate. The crystallographic orientation relationship between Cr underlayer and MgO substrate was Cr(211)[1$\bar{1}\bar{1}$], [$\bar{1}$11] || MgO(110)[1$\bar{1}$0].[6] After cooling the samples down to RT, $Fe_{100-x}Ni_x$ (x = 0, 30, 50, 60, 70, 80, 90, 100 at. %) alloy films of 10 nm thickness were formed on the Cr underlayers by alternative deposition of Fe and Ni layers. The layer structure was [Fe(1 – δ nm)/Ni(δ nm)]$_{10}$/Cr(10 nm)/MgO. The alloy formation and the film uniformity were checked by X-ray reflection. The Ni-Fe alloy composition was controlled by changing the δ value ($0 \leq \delta \leq 1$). The film composition was confirmed by energy dispersive X-ray spectroscopy and the errors were less than 3 at. % from the x values.

The film surface structure during growth process was observed by RHEED. The resulting film structure was investigated by $2\theta/\omega$-scan out-of-plane and pole-figure XRDs with Cu-Kα radiation (λ = 0.15418 nm). The surface morphology was observed by atomic force microscopy (AFM). The magnetization curves were measured by vibrating sample magnetometry.

3. Results and Discussion

3.1 Structure of $Fe_{100-x}Ni_x$ films ($0 \leq x \leq 50$ at. %)

Figures 1(a)–(c) and 2(a)–(c) show the RHEED patterns observed during formation of $Fe_{100-x}Ni_x$ films with x = 0–50 at. % on the Cr(211) underlayers. Here, two kinds of incident electron beam direction are used to identify the variant structure. The electron beam is parallel to MgO[1$\bar{1}$0] in Figs. 1(a)–(c), whereas that is parallel to MgO[001] in Figs. 2(a)–(c). MgO[001] is the

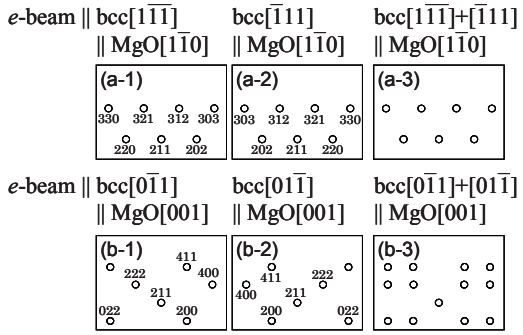

Fig. 3 Schematic diagrams of RHEED patterns simulated for bcc(211) crystal. The incident electron beam is parallel to (a-1) bcc[1$\bar{1}\bar{1}$], (a-2) bcc[$\bar{1}$11], (b-1) bcc[0$\bar{1}$1], or (b-2) bcc[01$\bar{1}$]. Schematic diagrams of (a-3) and (b-3) are drawn by overlapping (a-1) and (a-2) and by overlapping (b-1) and (b-2), respectively.

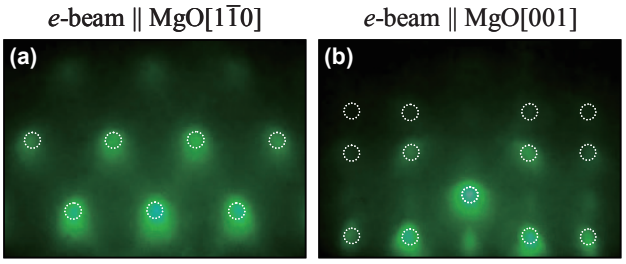

Fig. 4 RHEED patterns observed for a 10-nm-thick Fe film deposited on Cr(211) underlayer hetero-epitaxially grown on MgO(110) substrate [Figs. 1(a-4), 2(a-4)] overlapped with the reflection spots simulated for bcc(211) bi-crystal [Figs. 3(a-3), (b-3)]. The incident electron beam is parallel to (a) bcc[1$\bar{1}\bar{1}$]+bcc[$\bar{1}$11] || MgO[1$\bar{1}$0] or (b) bcc[0$\bar{1}$1]+bcc[01$\bar{1}$] || MgO[001].

direction rotated around the film normal by 90° with respect to MgO[1 $\bar{1}$ 0]. Clear RHEED patterns are observed from the beginnings till the ends of film formation. The films are epitaxially growing on the underlayers for the compositional range.

Possible diffraction patterns were calculated for bcc (*A*2) crystal. Figures 3(a-1)–(b-2) show the schematic diagrams of diffraction patterns of bcc(211) crystal simulated by making the incident electron beam parallel to bcc[1$\bar{1}\bar{1}$], bcc[$\bar{1}$11], bcc[0$\bar{1}$1], or bcc[01$\bar{1}$]. bcc[1$\bar{1}\bar{1}$] or bcc[$\bar{1}$11] is the direction rotated around the film normal by 90° with respect to bcc[0$\bar{1}$1] or bcc[01$\bar{1}$]. The experimental RHEED data shown in Figs. 1(a)–(c) (*e*-beam || MgO[1$\bar{1}$0]) are in agreement with both simulation results shown in Fig. 3(a-1) (*e*-beam || bcc[1$\bar{1}\bar{1}$]) and Fig. 3(a-2) (*e*-beam || bcc[$\bar{1}$11]). However, the observed RHEED patterns shown in Figs. 2(a)–(c) (*e*-beam || MgO[001]) are partially matching with the calculated patterns of Fig. 3(b-1) (*e*-beam || bcc[0$\bar{1}$1]) and Fig. 3(b-2) (*e*-beam || bcc[01$\bar{1}$]). Therefore, there is a possibility that bcc(211) bi-crystal is formed on the underlayer. Figures 3(a-3) and (b-3) are the schematic diagrams obtained by overlapping Figs. 3(a-1) and (a-2) and by overlapping Figs. 3(b-1) and (b-2), respectively.

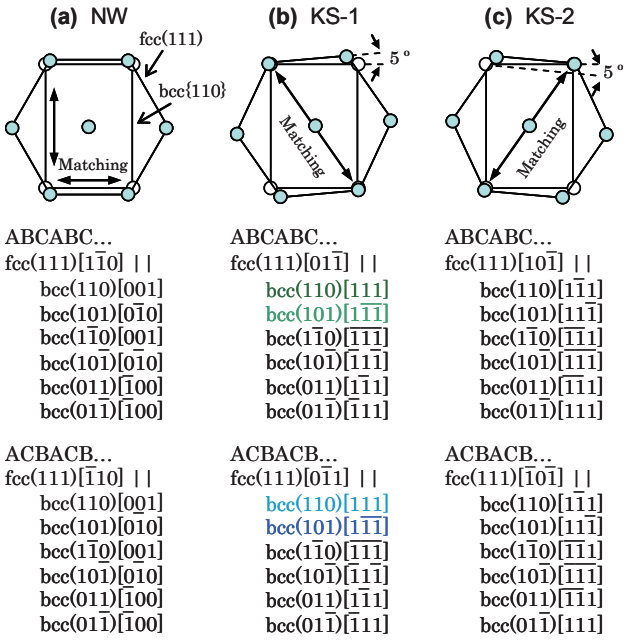

Fig. 5 Schematic diagrams and crystallographic orientation relationships of (a) NW, (b) KS-1, and (c) KS-2.

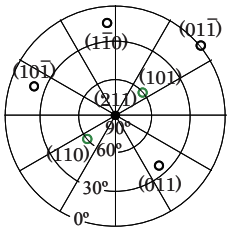

Fig. 6 Pole-figure map showing the configurations of bcc{110} planes around bcc(211) pole.

The observed RHEED patterns agree very well with the overlapped patterns of Figs. 3(a-3) and (b-3), as shown in Fig. 4. The crystallographic orientation relationships between bcc(211) crystal and MgO(110) substrate are thus determined as follows,

bcc-$Fe_{100-x}Ni_x$(211)[1$\bar{1}\bar{1}$] || Cr(211)[1$\bar{1}\bar{1}$], [$\bar{1}$11]
|| MgO(110)[1$\bar{1}$0], (Type I)

bcc-$Fe_{100-x}Ni_x$(211)[$\bar{1}$11] || Cr(211)[1$\bar{1}\bar{1}$], [$\bar{1}$11]
|| MgO(110)[1$\bar{1}$0]. (Type II)

The films consist of two bcc(211) variants whose orientations are rotated around the film normal by 180° each other.

3.2 Structure of $Fe_{100-x}Ni_x$ films ($60 \leq x \leq 70$ at. %)

Figures 1[(d), (e)] and 2[(d), (e)] show the RHEED patterns observed for $Fe_{40}Ni_{60}$ and $Fe_{30}Ni_{70}$ films. RHEED patterns corresponding to the simulated diffraction patterns from bcc(211) bi-crystal [Figs. 3(a-3), (b-3)] are observed for the $Fe_{40}Ni_{60}$ film thinner than 2

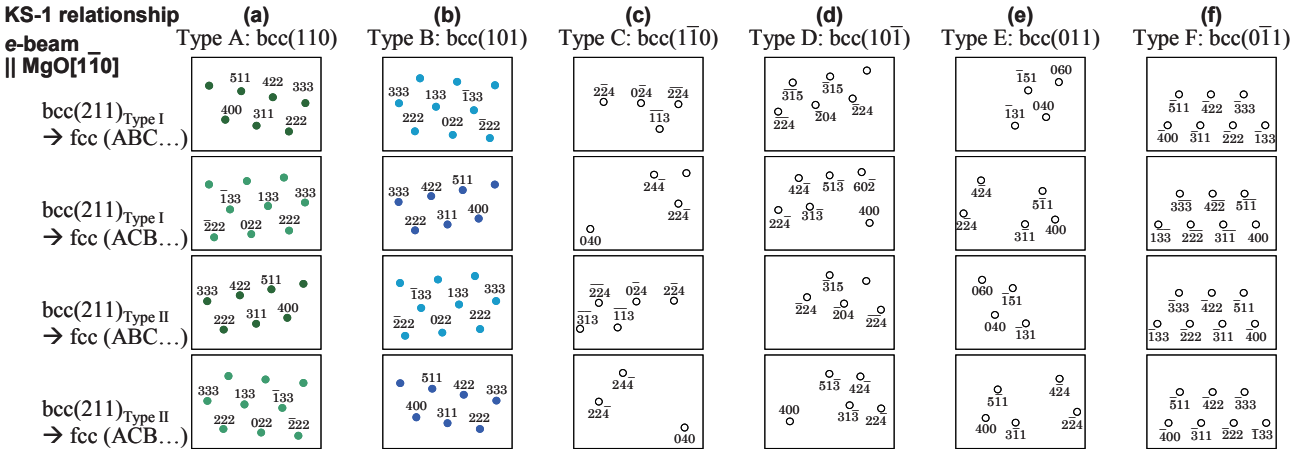

Fig. 7 Schematic diagrams of RHEED patterns simulated for fcc crystals with the atomic stacking sequences of ABCABC… and ACBACB… along fcc[111] transformed from bcc(211) crystals with I- and II-type epitaxial orientation relationships through atomic displacements parallel to (a) bcc(110), (b) bcc(101), (c) bcc(011), (d) bcc(10$\bar{1}$), (e) bcc(1$\bar{1}$0), and (f) bcc(0$\bar{1}$1) planes in the KS-1 relationship. The incident electron beam is parallel to MgO[1$\bar{1}$0].

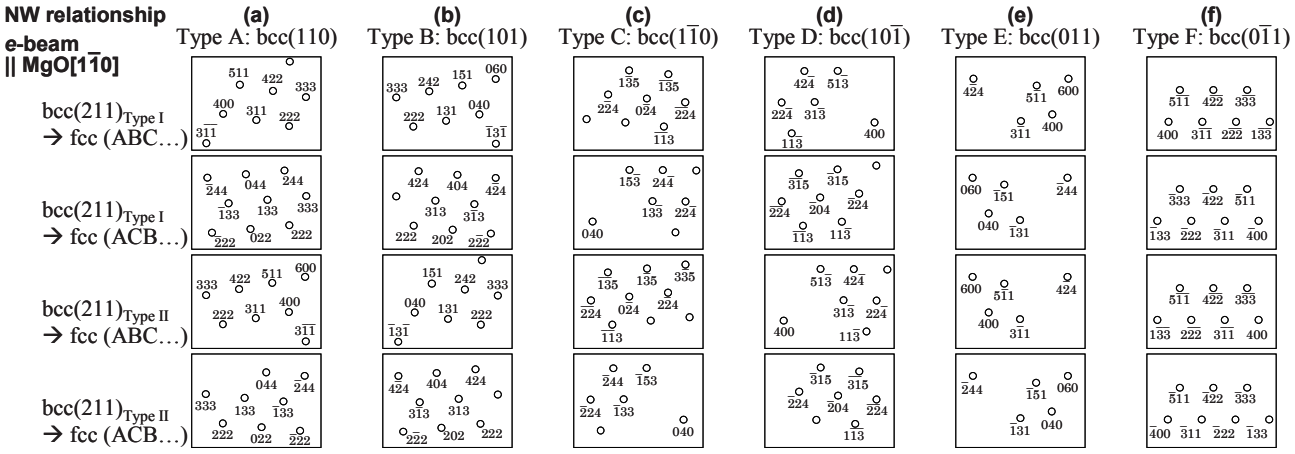

Fig. 8 Schematic diagrams of RHEED patterns simulated for fcc crystals with the atomic stacking sequences of ABCABC… and ACBACB… along fcc[111] transformed from bcc(211) crystals with I- and II-type epitaxial orientation relationships through atomic displacements parallel to (a) bcc(110), (b) bcc(101), (c) bcc(011), (d) bcc(10$\bar{1}$), (e) bcc(1$\bar{1}$0), and (f) bcc(0$\bar{1}$1) planes in the NW relationship. The incident electron beam is parallel to MgO[1$\bar{1}$0].

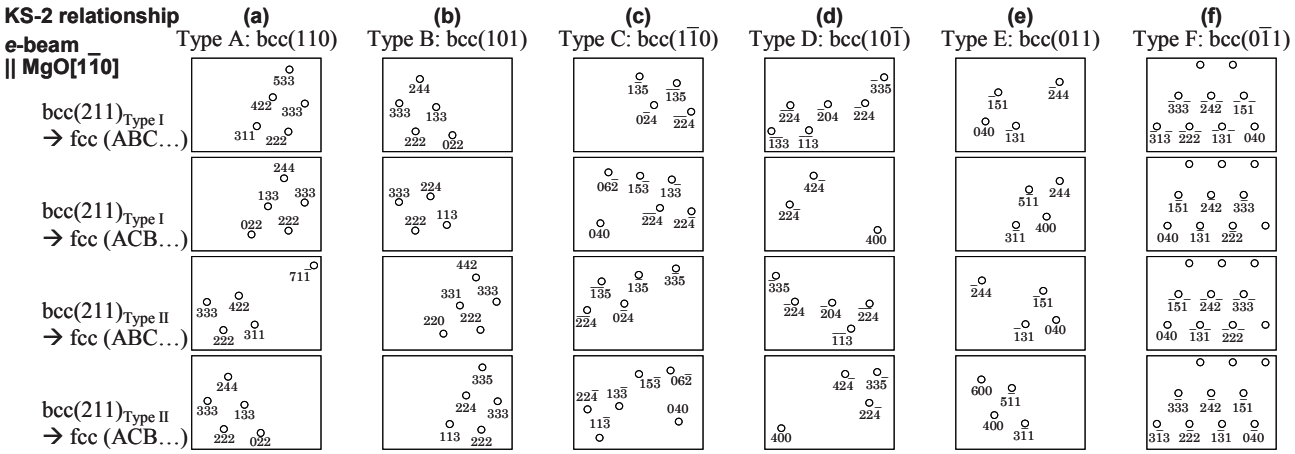

Fig. 9 Schematic diagrams of RHEED patterns simulated for fcc crystals with the atomic stacking sequences of ABCABC… and ACBACB… along fcc[111] transformed from bcc(211) crystals with I- and II-type epitaxial orientation relationships through atomic displacements parallel to (a) bcc(110), (b) bcc(101), (c) bcc(011), (d) bcc(10$\bar{1}$), (e) bcc(1$\bar{1}$0), and (f) bcc(0$\bar{1}$1) planes in the KS-2 relationship. The incident electron beam is parallel to MgO[1$\bar{1}$0].

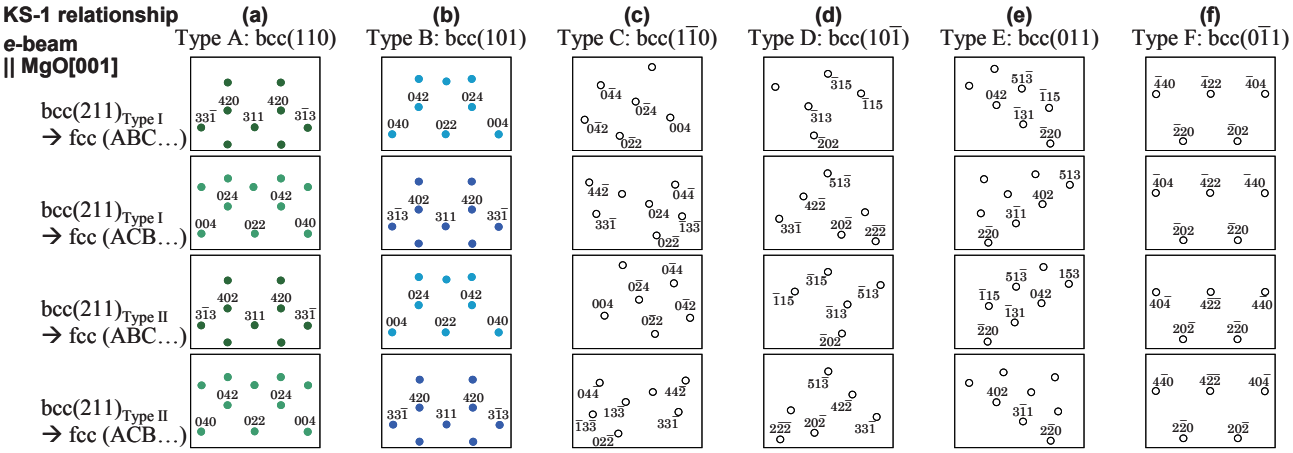

Fig. 10 Schematic diagrams of RHEED patterns simulated for fcc crystals with the atomic stacking sequences of ABCABC… and ACBACB… along fcc[111] transformed from bcc(211) crystals with I- and II-type epitaxial orientation relationships through atomic displacements parallel to (a) bcc(110), (b) bcc(101), (c) bcc(011), (d) bcc(10$\bar{1}$), (e) bcc(1$\bar{1}$0), and (f) bcc(0$\bar{1}$1) planes in the KS-1 relationship. The incident electron beam is parallel to MgO[001].

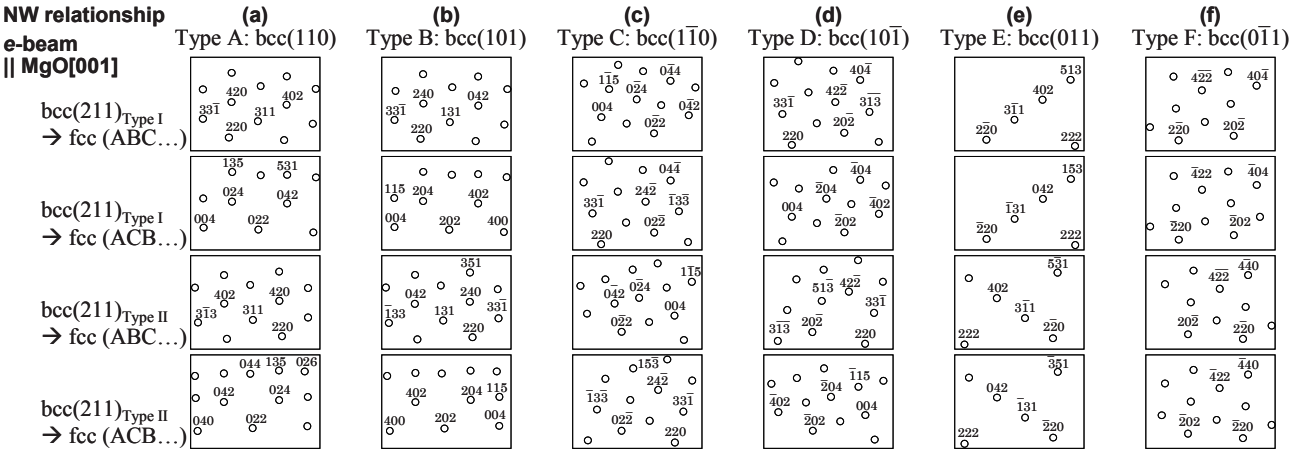

Fig. 11 Schematic diagrams of RHEED patterns simulated for fcc crystals with the atomic stacking sequences of ABCABC… and ACBACB… along fcc[111] transformed from bcc(211) crystals with I- and II-type epitaxial orientation relationships through atomic displacements parallel to (a) bcc(110), (b) bcc(101), (c) bcc(011), (d) bcc(10$\bar{1}$), (e) bcc(1$\bar{1}$0), and (f) bcc(0$\bar{1}$1) planes in the NW relationship. The incident electron beam is parallel to MgO[001].

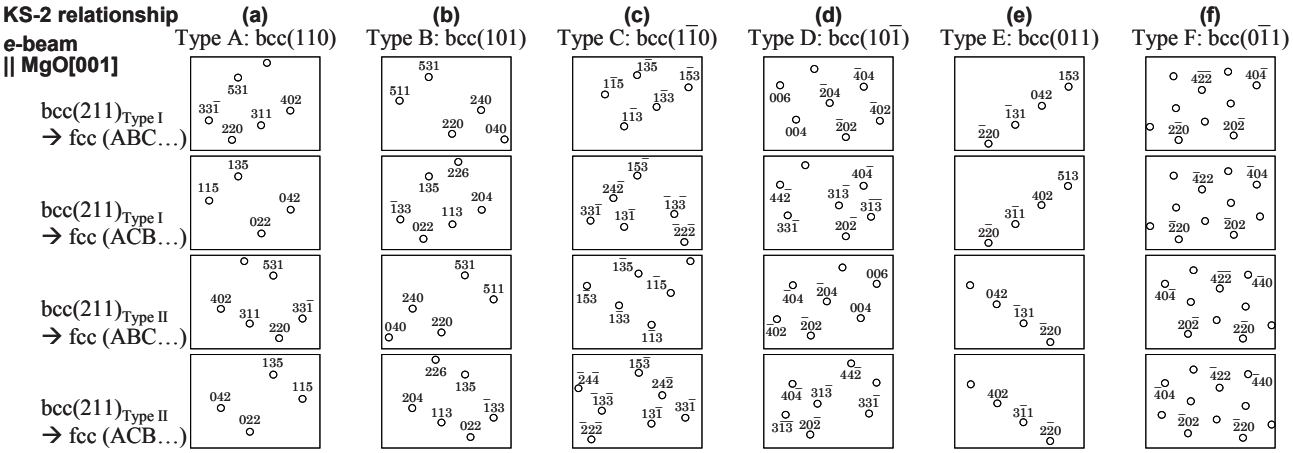

Fig. 12 Schematic diagrams of RHEED patterns simulated for fcc crystals with the atomic stacking sequences of ABCABC… and ACBACB… along fcc[111] transformed from bcc(211) crystals with I- and II-type epitaxial orientation relationships through atomic displacements parallel to (a) bcc(110), (b) bcc(101), (c) bcc(011), (d) bcc(10$\bar{1}$), (e) bcc(1$\bar{1}$0), and (f) bcc(0$\bar{1}$1) planes in the KS-2 relationship. The incident electron beam is parallel to MgO[001].

nm [Figs. 1(d-1)–(d-2), 2(d-1)–(d-2)] and the $Fe_{30}Ni_{70}$ film thinner than 1 nm [Figs. 1(e-1), 2(e-1)]. With further increasing the thickness [Figs. 1(d-3)–(d-4), 1(e-2)–(e-4), 2(d-3)–(d-4), 2(e-2)–(e-4)], RHEED spots become broader and diffraction spots other than bcc crystal appear for both films, indicating that phase transformation is taking place. The thickness stability of bcc crystal formation is decreased as the x value increases from 50 to 70 at. %.

When a bulk bcc material transforms into fcc structure, there are two possible crystallographic orientation relationships of Nishiyama-Wasserman[15,16] (NW) and Kurdjumov-Sachs[17] (KS),

$$\begin{aligned}&\mathrm{fcc}(111)[1\bar{1}0]_{\mathrm{ABCABC\ldots}},\ \mathrm{fcc}(111)[\bar{1}10]_{\mathrm{ACBACB\ldots}}\\ &\quad\parallel\ \mathrm{bcc}(110)[001],\ \mathrm{bcc}(101)[0\bar{1}0],\ \mathrm{bcc}(1\bar{1}0)[001],\\ &\qquad\mathrm{bcc}(10\bar{1})[0\bar{1}0],\ \mathrm{bcc}(011)[\bar{1}00],\ \mathrm{bcc}(01\bar{1})[\bar{1}00],\quad\text{(NW)}\end{aligned}$$

$$\begin{aligned}&\mathrm{fcc}(111)[01\bar{1}]_{\mathrm{ABCABC\ldots}},\ \mathrm{fcc}(111)[0\bar{1}1]_{\mathrm{ACBACB\ldots}}\\ &\quad\parallel\ \mathrm{bcc}(110)[111],\ \mathrm{bcc}(101)[1\bar{1}\bar{1}],\ \mathrm{bcc}(1\bar{1}0)[\bar{1}\bar{1}\bar{1}],\\ &\qquad\mathrm{bcc}(10\bar{1})[\bar{1}\bar{1}\bar{1}],\ \mathrm{bcc}(011)[1\bar{1}1],\ \mathrm{bcc}(01\bar{1})[\bar{1}11],\quad\text{(KS-1)}\end{aligned}$$

$$\begin{aligned}&\mathrm{fcc}(111)[10\bar{1}]_{\mathrm{ABCABC\ldots}},\ \mathrm{fcc}(111)[\bar{1}01]_{\mathrm{ACBACB\ldots}}\\ &\quad\parallel\ \mathrm{bcc}(110)[111],\ \mathrm{bcc}(101)[1\bar{1}\bar{1}],\ \mathrm{bcc}(1\bar{1}0)[\bar{1}\bar{1}\bar{1}],\\ &\qquad\mathrm{bcc}(10\bar{1})[\bar{1}\bar{1}\bar{1}],\ \mathrm{bcc}(011)[1\bar{1}1],\ \mathrm{bcc}(01\bar{1})[\bar{1}11].\quad\text{(KS-2)}\end{aligned}$$

The phase transformation occurs through atomic displacements from bcc(110), bcc(101), bcc(011), bcc(10$\bar{1}$), bcc(1$\bar{1}$0), and bcc(0$\bar{1}$1) close-packed planes to fcc(111) plane, as shown in Fig. 5. The configurations of bcc{110} planes in a bcc crystal with the (211) plane parallel to the substrate surface are shown in the pole-figure map of Fig. 6.

Figures 7–12 show the schematic diagrams of RHEED patterns simulated for fcc ($A1$) crystals with the atomic stacking sequences of ABCABC… and ACBACB… along fcc[111] transformed from bcc(211) crystals with I- and II-type orientation relationships through atomic displacements parallel to bcc{110} planes in the KS-1 [Figs. 7, 10], the NW [Figs. 8, 11], and the KS-2 [Figs. 9, 12] relationships. Figures 13(a)–(f) are drawn by overlapping all the schematic diagrams shown in Figs. 7–12, respectively. Here, the electron beam is parallel to MgO[1$\bar{1}$0] in Figs. 13(a)–(c), whereas that is parallel to MgO[001] in Figs. 13(d)–(f). The RHEED patterns observed for the $Fe_{40}Ni_{60}$ film thicker than 5 nm [Figs. 1(d-3)–(d-4), 2(d-3)–(d-4)] and the $Fe_{30}Ni_{70}$ film thicker than 2 nm [Figs. 1(e-2)–(e-4), 2(e-2)–(e-4)] are different from any patterns shown in Fig. 13. The bcc{110} slide planes where the phase transformation occurs are considered to be influenced by the strain caused by accommodation of the lattice misfit between film and underlayer[18].

Figures 14(a)–(f) are obtained by overlapping the schematic diagrams of patterns simulated for fcc crystals transformed through atomic displacements parallel to bcc(110) and bcc(101) planes [Figs. 7[(a), (b)], 8[(a), (b)], 9[(a), (b)], 10[(a), (b)], 11[(a), (b)], 12[(a), (b)]].

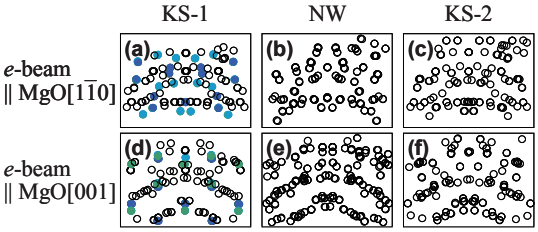

Fig. 13 Schematic diagrams of RHEED patterns simulated for fcc crystals transformed through atomic displacements from bcc(110), bcc(101), bcc(011), bcc(10$\bar{1}$), bcc(1$\bar{1}$0), and bcc(0$\bar{1}$1) planes to fcc(111) plane in [(a), (d)] the KS-1, [(b), (e)] the NW, and [(c), (f)] the KS-2 relationships. The incident electron beam is parallel to (a)–(c) MgO[1$\bar{1}$0] or (d)–(f) MgO[001]. The schematic diagrams of (a)–(f) are drawn by overlapping all the schematic diagrams shown in Figs. 7–12, respectively.

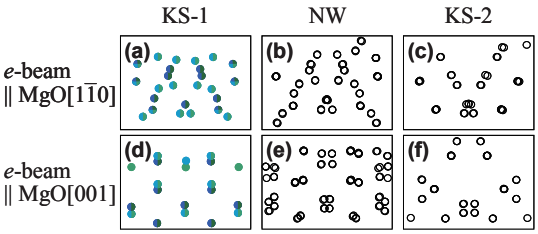

Fig. 14 Schematic diagrams of RHEED patterns simulated for fcc crystals transformed through atomic displacements from bcc(110) and bcc(101) planes to fcc(111) plane in [(a), (d)] the KS-1, [(b), (e)] the NW, and [(c), (f)] the KS-2 relationships. The incident electron beam is parallel to (a)–(c) MgO[1$\bar{1}$0] or (d)–(f) MgO[001]. The schematic diagrams of (a)–(f) are drawn by overlapping all the schematic diagrams shown in Figs. 7[(a), (b)]–12[(a), (b)], respectively.

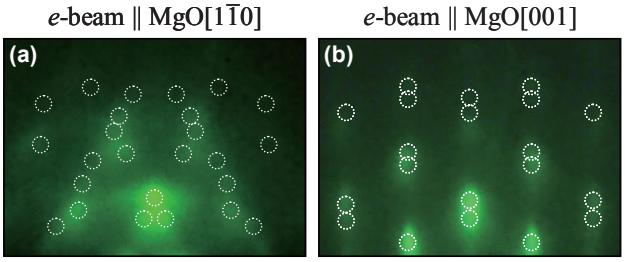

Fig. 15 RHEED patterns observed for a 10-nm-thick $Fe_{30}Ni_{70}$ film deposited on Cr(211) underlayer hetero-epitaxially grown on MgO(110) substrate [Figs. 1(e-4), 2(e-4)] overlapped with the reflection spots simulated for fcc crystals transformed through atomic displacements from bcc(110) and bcc(101) planes to fcc(111) plane in the KS-1 relationship [Figs. 14(a), (d)]. The incident electron beam is parallel to (a) MgO[1$\bar{1}$0] or (b) MgO[001].

The RHEED patterns observed for the $Fe_{40}Ni_{60}$ film thicker than 5 nm [Figs. 1(d-3)–(d-4), 2(d-3)–(d-4)] and the $Fe_{30}Ni_{70}$ film thicker than 2 nm [Figs. 1(e-2)–(e-4), 2(e-2)–(e-4)] are in agreement with the simulated patterns of Figs. 14(a) and (d), as shown in Fig. 15. The

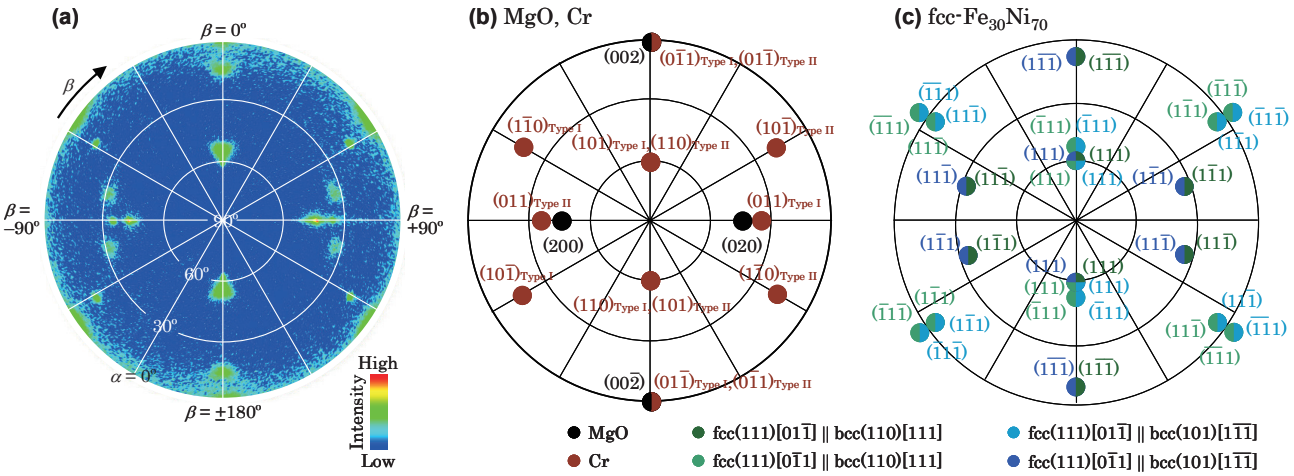

Fig. 16 (a) Pole-figure XRD pattern measured for a 40-nm-thick $Fe_{30}Ni_{70}$ film deposited on Cr(211) underlayer hetero-epitaxially grown on MgO(110) substrate. The diffraction angle of $2\theta B$ is fixed at 44°. The intensity is shown in logarithmic scale. [(b), (c)] Schematic diagrams obtained (b) by overlapping the diffraction patterns simulated for MgO(110) substrate and Cr(211) underlayer and (c) by overlapping the patterns calculated for the fcc crystals transformed from bcc structure in the crystallographic orientation relationships determined by RHEED.

result shows that the phase transformation is not taking place through atomic displacements from six bcc{110} planes but from bcc(110) and bcc(101) planes, which are 60° inclined from the perpendicular direction, in the KS-1 relationship.

When the bcc(211) epitaxial bicrystalline films transform into fcc structure through atomic displacements parallel to bcc(110) and bcc(101) planes in the KS relationship, the films consist of four fcc crystals. fcc(311) is 0.5° tilted from the substrate surface for the fcc crystals with the staking sequences of ABCABC… and ACBACB… along fcc[111] transformed from bcc(211) crystals with I- and II-type relationships through atomic displacements parallel to bcc(110) and bcc(101) planes, respectively. On the other hand, fcc(011) plane is 5° canted from the substrate surface for the fcc crystals with the staking sequences of ACBACB… and ABCABC… along fcc[111] transformed from bcc(211) crystals with I- and II-type relationships through atomic displacements parallel to bcc(110) and bcc(101) planes, respectively. These low-index planes of transformed fcc crystals tend to be more inclined from the substrate surface in the cases of NW and KS-2 relationships. Therefore, the phase transformation in the KS-1 relationship seems to be favored.

In order to confirm the phase transformation orientation relationships, pole-figure XRD was carried out. Figure 16(a) shows the pole-figure XRD pattern of a 40-nm-thick $Fe_{30}Ni_{70}$ film deposited on Cr(211) underlayer hetero-epitaxially grown on MgO(110) substrate. Here, the film thickness of 40 nm is employed so that the reflections from transformed fcc crystals are detected more strongly. The diffraction angle of $2\theta B$ is fixed at 44°, where MgO{200}, Cr{110}, and fcc-$Fe_{30}Ni_{70}${111} reflections are expected to be detectable. Figures 16(b) and (c), respectively, show the schematic diagrams obtained by overlapping the diffraction patterns simulated for MgO(110) substrate and Cr(211) underlayer and by overlapping the patterns calculated for the fcc crystals transformed from bcc structure in the crystallographic orientation relationships determined by RHEED. The measured pole-figure XRD pattern of Fig. 16(a) apparently agrees with an overlap of the simulated patterns of Figs. 16(b) and (c). The pole-figure XRD confirms the orientation relationships determined by RHEED.

3.3 Structure of $Fe_{100-x}Ni_x$ films ($80 \leq x \leq 100$ at. %)

Figures 1[(g), (h)] and 2[(g), (h)] show the RHEED patterns observed for $Fe_{10}Ni_{90}$ and Ni films. Diffraction patterns from hcp(1$\bar{1}$00) surface shown in the schematic diagrams of Fig. 17 are overlapped with those from bcc(211) surface [Figs. 3(a-3), (b-3)] for the $Fe_{10}Ni_{90}$ film thinner than 1 nm [Figs. 1(g-1), 2(g-1)] and the Ni film thinner than 5 nm [Figs. 1(h-1)–(h-3), 2(h-1)–(h-3)], as shown in Fig. 18. Therefore, these films are composed of a mixture of hcp(1$\bar{1}$00) and bcc(211) crystals. $Fe_{10}Ni_{90}$ and Ni crystals with metastable hcp structure are stabilized through hetero-epitaxial growth on Cr(211) underlayer, similar to the cases of previous studies[5–8]. The crystallographic orientation relationship between hcp-$Fe_{100-x}Ni_x$(1$\bar{1}$00) crystal and Cr underlayer is

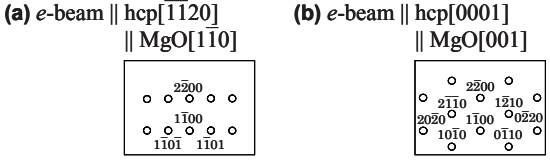

Fig. 17 Schematic diagrams of RHEED patterns simulated for hcp(1$\bar{1}$00) crystal. The incident electron beam is parallel to (a) hcp[11̄20] or (b) hcp[0001].

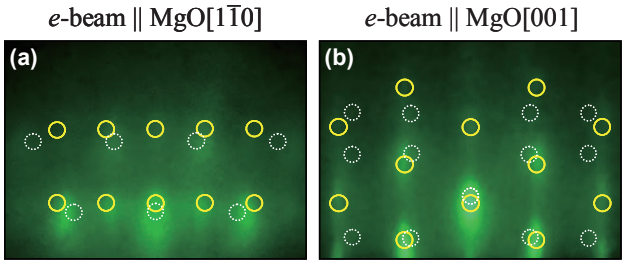

Fig. 18 RHEED patterns observed for a 1-nm-thick $Fe_{10}Ni_{90}$ film deposited on Cr(211) underlayer hetero-epitaxially grown on MgO(110) substrate [Figs. 1(g-1), 2(g-1)] overlapped with the reflection spots simulated for hcp(1$\bar{1}$00) [Fig. 17] and bcc(211) [Figs. 3(a-3), (b-3)] crystals. The incident electron beam is parallel to (a) MgO[1$\bar{1}$0] or (b) MgO[001]. The diffraction patterns consisting of yellow solid and white dotted circles correspond to Fig. 17 and Figs. 3[(a-3), (b-3)], respectively.

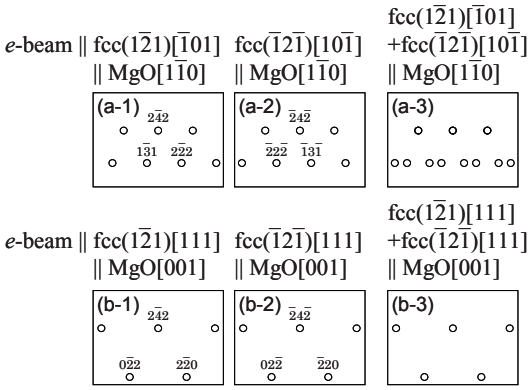

Fig. 19 Schematic diagrams of RHEED patterns simulated for fcc crystals with the atomic stacking sequences of [(a-1), (b-1)] ABCABC… and [(a-2), (b-2)] ACBACB… along fcc[111] transformed from hcp(1$\bar{1}$00) crystal with III-type orientation relationship through atomic displacement parallel to hcp(0001) plane in the SN relationship. The incident electron beam is parallel to (a) MgO[1$\bar{1}$0] or (b) MgO[001]. Schematic diagrams of (a-3) and (b-3) are drawn by overlapping (a-1) and (a-2) and by overlapping (b-1) and (b-2), respectively.

determined by RHEED as

hcp-$Fe_{100-x}Ni_x$(1$\bar{1}$00)[11$\bar{2}$0] || Cr(211)[1$\bar{1}$$\bar{1}$], [$\bar{1}$11]
|| MgO(110)[1$\bar{1}$0]. (Type III)

As the thickness further increases [Figs. 1(g-2)–(g-4), 1(h-4), 2(g-2)–(g-4), 2(h-4)], RHEED spots become broader, suggesting that the phase transformations from hcp and bcc crystals to fcc structure are taking place. The details of hcp-fcc phase transformation in hcp(1$\bar{1}$00) film are shown in our previous paper[6]. The hcp-fcc transformation occurred through atomic displacement from hcp(0001) to fcc(111) plane. The crystallographic orientation relationship between hcp and fcc crystals was

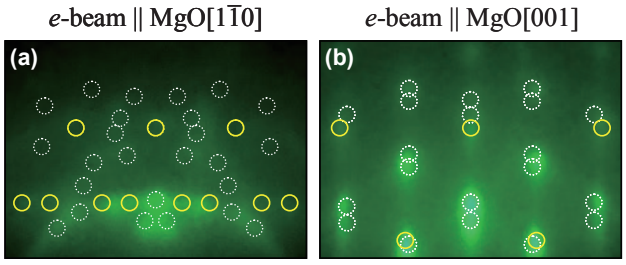

Fig. 20 RHEED patterns observed for a 10-nm-thick $Fe_{10}Ni_{90}$ film deposited on Cr(211) underlayer hetero-epitaxially grown on MgO(110) substrate [Figs. 1(g-4), 2(g-4)] overlapped with the reflection spots calculated for fcc crystals transformed through atomic displacements from hcp(0001) to fcc(111) plane in the SN relationship [Figs. 19(a-3), (b-3)] and the reflection spots simulated for fcc crystals transformed through atomic displacements from bcc(110) and bcc(101) planes to fcc(111) plane in the KS-1 relationship [Figs. 14(a), (d)]. The incident electron beam is parallel to (a) MgO[1$\bar{1}$0] or (b) MgO[001]. The diffraction patterns consisting of yellow solid and white dotted circles correspond to Fig. 19[(a-3), (b-3)]] and Figs. 14[(a-3), (b-3)], respectively.

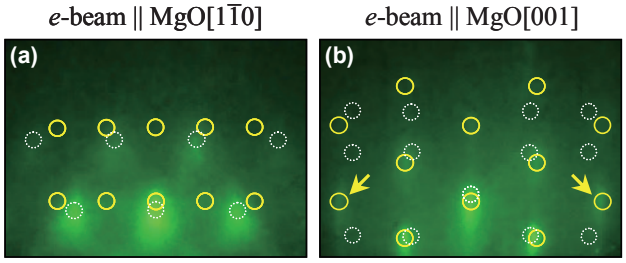

Fig. 21 RHEED patterns observed for a 1-nm-thick $Fe_{20}Ni_{80}$ film deposited on Cr(211) underlayer hetero-epitaxially grown on MgO(110) substrate [Figs. 1(f-1), 2(f-1)] overlapped with the reflection spots simulated for hcp(1$\bar{1}$00) [Fig. 17] and bcc(211) [Figs. 3(a-3), (b-3)] crystals. The incident electron beam is parallel to (a) MgO[1$\bar{1}$0] or (b) MgO[001]. The diffraction patterns consisting of yellow solid and white dotted circles correspond to Fig. 17 and Figs. 3[(a-3), (b-3)], respectively.

fcc(1$\bar{2}$1)[$\bar{1}$01], fcc($\bar{1}$2$\bar{1}$)[10$\bar{1}$] || hcp(1$\bar{1}$00)[$\bar{1}$$\bar{1}$20]
|| Cr(211)[1$\bar{1}$$\bar{1}$], [$\bar{1}$11]
|| MgO(110)[1$\bar{1}$0], (SN)

which was similar to the Shoji-Nishiyama (SN) relationship[19,20].

Figure 19 shows the schematic diagrams of RHEED patterns calculated for fcc crystals transformed in the SN relationship. The RHEED patterns observed for the $Fe_{10}Ni_{90}$ film thicker than 2 nm [Figs. 1(g-2)–(g-4), 2(g-2)–(g-4)] and the Ni film of 10 nm thickness [Figs. 1(h-4), 2(h-4)] are considered to be consisting of the diffraction patterns of Figs. 14[(a), (d)] and 19[(a-3), (b-3)], as shown in Fig. 20.

Figures 1(f) and 2(f) show the RHEED patterns observed during $Fe_{20}Ni_{80}$ film formation. The RHEED

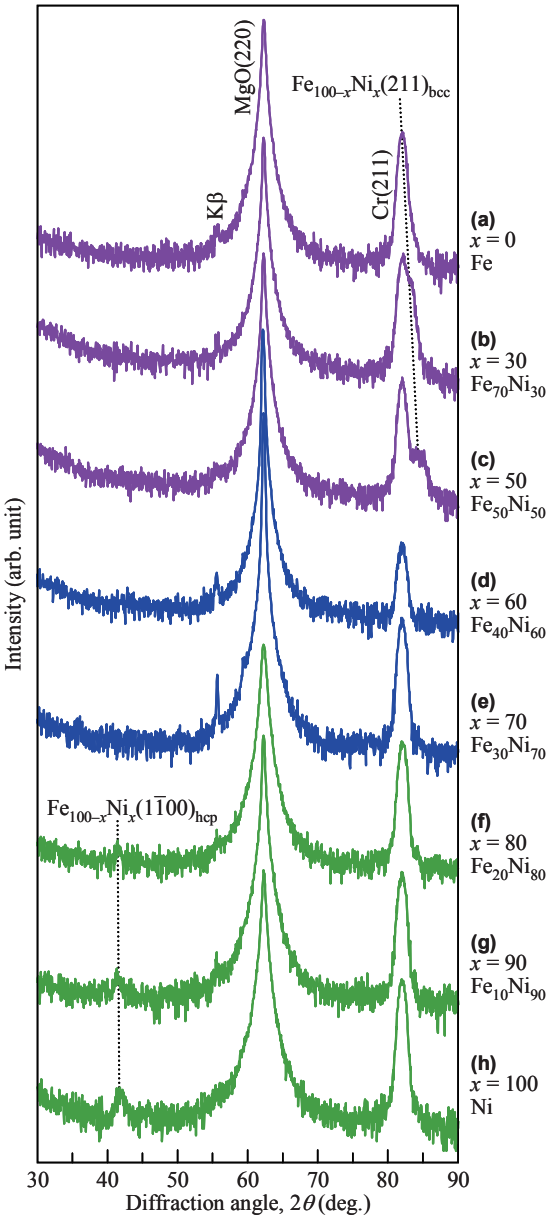

Fig. 22 Out-of-plane XRD patterns of (a) Fe, (b) $Fe_{70}Ni_{30}$, (c) $Fe_{50}Ni_{50}$, (d) $Fe_{40}Ni_{60}$, (e) $Fe_{30}Ni_{70}$, (f) $Fe_{20}Ni_{80}$, (g) $Fe_{10}Ni_{90}$, and (h) Ni films deposited on Cr(211) underlayers hetero-epitaxially grown on MgO(110) substrates. The intensity is shown in logarithmic scale.

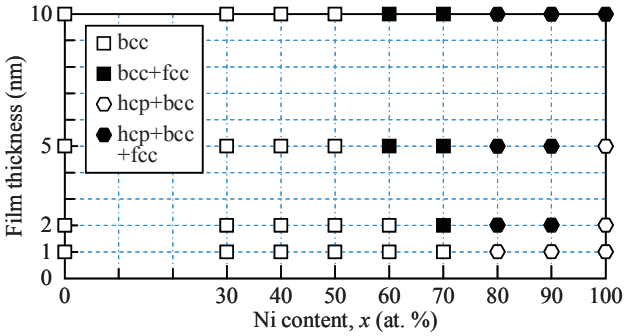

Fig. 23 Phase transformation map of $Fe_{100-x}Ni_x$ films.

patterns observed for the 1-nm-thick film [Figs. 1(f-1), 2(f-1)] seems to involve the reflection spots from hcp($1\bar{1}$00) crystal as shown in Fig. 21, though the reflection intensity of hcp($1\bar{1}$00) crystal is fairly weaker than that of bcc(211) crystal. With increasing the thickness beyond 2 nm [Figs. 1(f-2)–(f-4), 2(f-2)–(f-4)], the RHEED pattern changes to an overlap of diffraction patterns from fcc crystals transformed from bcc and hcp structures [Figs. 14[(a), (d)], 19[(a-3), (b-3)]].

Figure 22 shows the out-of-plane XRD patterns measured for the $Fe_{100-x}Ni_x$ films of 10 nm thickness with different compositions. bcc-$Fe_{100-x}Ni_x$(211) reflections are observed for the Fe, the $Fe_{70}Ni_{30}$, and the $Fe_{50}Ni_{50}$ films (x = 0–50 at. %), while those are absent for the $Fe_{40}Ni_{60}$ and the $Fe_{30}Ni_{70}$ films (x = 60–70 at. %) where the bcc-fcc phase transformation is taking place. hcp-$Fe_{100-x}Ni_x(1\bar{1}00)$ reflections are recognized not only for the $Fe_{10}Ni_{90}$ and the Ni films (x = 90–100 at. %) but also for the $Fe_{20}Ni_{80}$ film (x = 80 at. %). As the x value increases from 80 to 100 at. %, the intensity of hcp($1\ \bar{1}\ 00$) reflection increases, indicating that the volume of hcp crystal nucleated on Cr(211) underlayer is increased with increasing the Ni content. By considering the RHEED and the XRD data, the phase transformation map of $Fe_{100-x}Ni_x$ films is determined as shown in Fig. 23.

3.4 Surface morphology and magnetic property

Figure 24 shows the AFM images observed for the $Fe_{100-x}Ni_x$ films deposited on Cr(211) underlayers. These

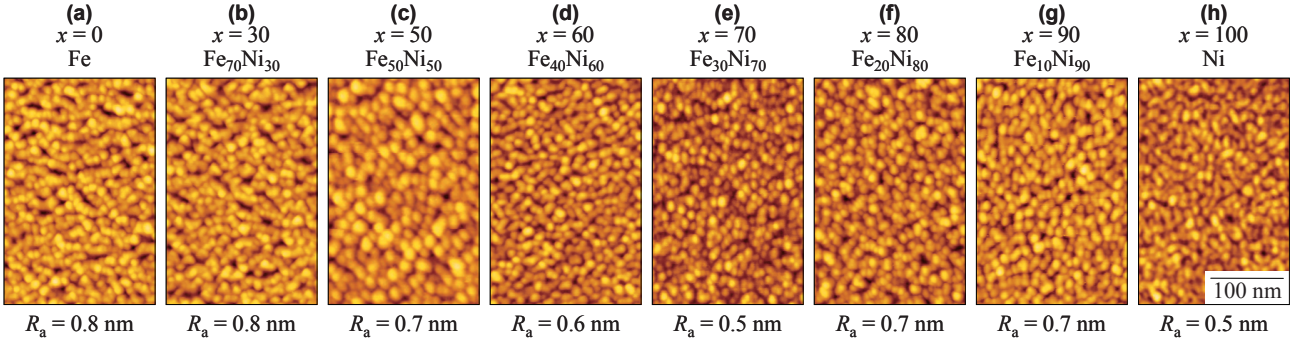

Fig. 24 AFM images observed for (a) Fe, (b) $Fe_{70}Ni_{30}$, (c) $Fe_{50}Ni_{50}$, (d) $Fe_{40}Ni_{60}$, (e) $Fe_{30}Ni_{70}$, (f) $Fe_{20}Ni_{80}$, (g) $Fe_{10}Ni_{90}$, and (h) Ni films deposited on Cr(211) underlayers hetero-epitaxially grown on MgO(110) substrates.

films have flat surfaces with the arithmetical mean roughness (R_a) values lower than 1 nm.

Figure 25 shows the magnetization curves measured for the $Fe_{100-x}Ni_x$ films. The magnetic field is applied along MgO[1$\bar{1}$0], MgO[001], or the direction rotated around the film normal by 51° with respect to MgO[1$\bar{1}$0], which is the direction obtained by inclining bcc[010] of bcc(211) crystals with I- and II-type orientation relationships to the film plane. The effective easy magnetization direction is observed along MgO[001] for the films with x = 0–70 at. %, whereas that is recognized along MgO[1$\bar{1}$0] for the films with x = 80–100 at. %. The magnetic properties seem to be delicately influenced by the crystal structure, the film composition, the configuration of transformed fcc crystals, etc.

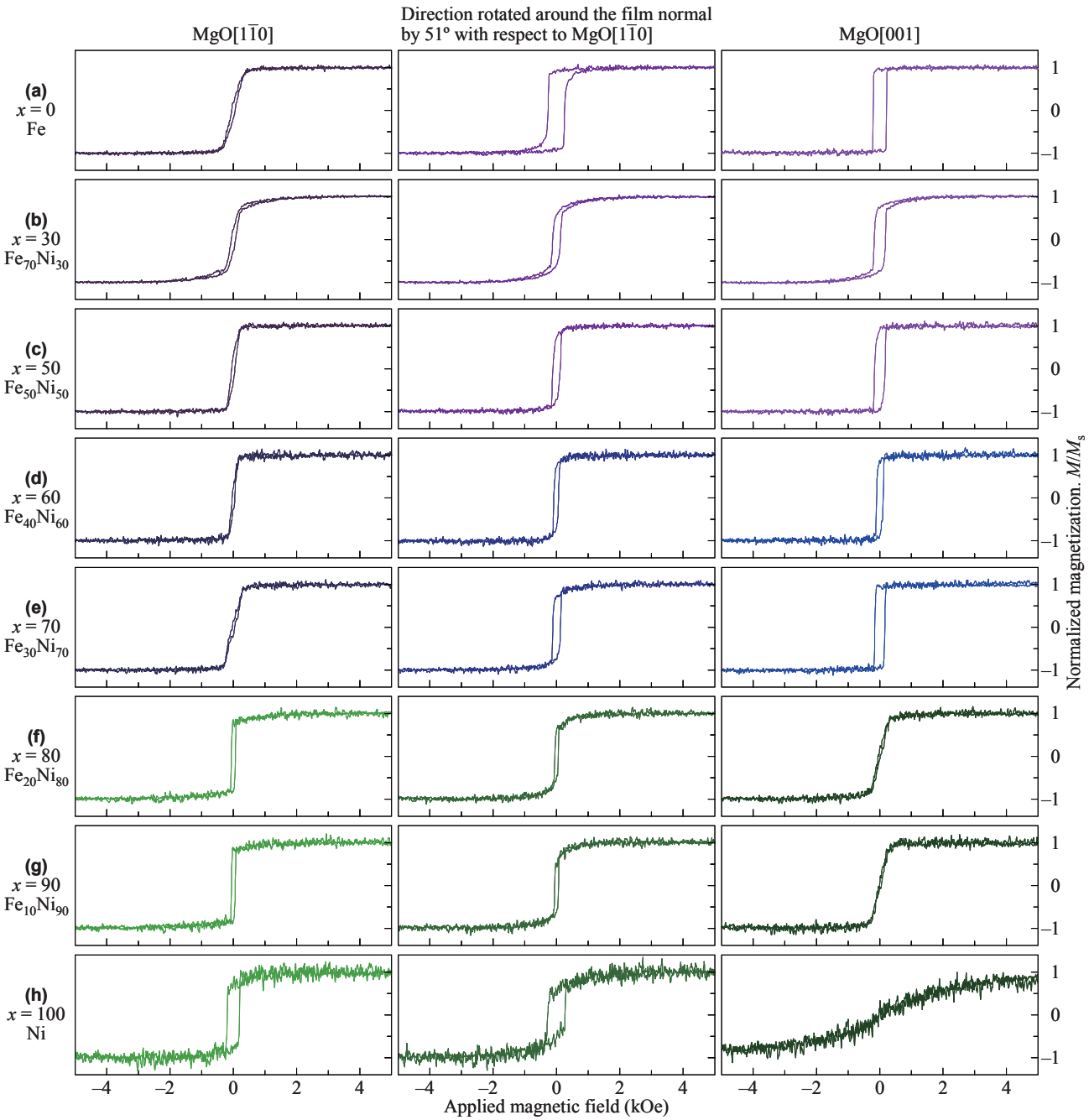

Fig. 25 Magnetization curves measured for (a) Fe, (b) $Fe_{70}Ni_{30}$, (c) $Fe_{50}Ni_{50}$, (d) $Fe_{40}Ni_{60}$, (e) $Fe_{30}Ni_{70}$, (f) $Fe_{20}Ni_{80}$, (g) $Fe_{10}Ni_{90}$, and (h) Ni films deposited on Cr(211) underlayers hetero-epitaxially grown on MgO(110) substrates. The magnetic field is applied along MgO[1$\bar{1}$0], MgO[001], or the direction rotated around the film normal by 51° with respect to MgO[1$\bar{1}$0], which is the direction obtained by inclining bcc[010] of bcc(211) crystals with I- and II-type orientation relationships to the film plane.

4. Conclusion

$Fe_{100-x}Ni_x$ alloy epitaxial films of 10 nm thickness are prepared on Cr(211) underlayers by varying the composition in the full range of x = 0–100 at. %. The film growth behavior and the crystallographic properties are investigated by RHEED and XRD. bcc(211) crystal nucleates on the underlayer for the $Fe_{100-x}Ni_x$ films with x = 0–70 at. %, whereas hcp($1\bar{1}00$) crystal coexists with bcc(211) crystal in the cases of x = 80–100 at. %. With increasing the thickness, the bcc(211) and/or the hcp($1\bar{1}00$) crystals start to transform into fcc structure for the films with $x \geq 60$ at. %. As the x value increases, the critical thickness up to which bcc crystal stability is maintained decreases, whereas that for hcp crystal increases. The bcc-fcc and the hcp-fcc phase transformations occur through atomic displacements from bcc(110) and bcc(101) close-packed planes and from hcp(0001) close-packed plane to fcc(111) close-packed plane, respectively. The crystallographic orientation relationships are similar to the Kurdjumov-Sachs and the Shoji-Nishiyama relationships.

Acknowledgments A part of this work was supported by JSPS KAKENHI Grant Numbers 25420294 and 26820117 and Chuo University Grant for Special Research.

References

1) X. -G. Zhang and W. H. Butler: *Phys. Rev. B*, **70**, 172407 (2004).
2) J. P. Velev, K. D. Belashchenko, D. A. Stewart, M. van Schifgaarde, S. S. Jaswal, and E. Y. Tsymbal: *Phys. Rev. Lett.*, **95**, 216601 (2005).
3) S. Yuasa, A. Fukushima, H. Kubota, Y. Suzuki, and K. Ando: *Appl. Phys. Lett.*, **89**, 042505 (2006).
4) T. B. Massalski, H. Okamoto, P. R. Subramanian, and L. Kacprzak: *Binary Alloy Phase Diagrams* (ASM International, Ohio, 1990).
5) J. C. A. Huang, Y. M. Yu, C. C. Yu, C. H. Tsao, and C. H. Lee: *Phys. Rev. B*, **57**, 11517 (1998).
6) M. Ohtake, Y. Sato, J. Higuchi, and M. Futamoto: *J. Phys.: Conf. Ser.*, **266**, 012122 (2011).
7) J. Higuchi, M. Ohtake, Y. Sato, and M. Futamoto: *J. Phys.: Conf. Ser.*, **303**, 012053 (2011).
8) J. Higuchi, M. Ohtake, Y. Sato, F. Kirino, and M. Futamoto: *Thin Solid Films*, **519**, 8347 (2011).
9) M. Ohtake, T. Yanagawa, J. Higuchi, and M. Futamoto: *EPJ Web Conf.*, **40**, 08004 (2013).
10) P. Bayle-Guillemaud and J. Thibault: *Philos. Mag. A*, **77**, 475 (1998).
11) M. Ohtake, Y. Sato, J. Higuchi, T. Tanaka, F. Kirino, and M. Futamoto: *Jpn. J. Appl. Phys.*, **50**, 103001 (2011).
12) W. Tian, H. P. Sun, X. Q. Pan, J. H. Yu, M. Yeadon, C. B. Boothroyd, Y. P. Feng, R. A. Lukaszew, and R. Clarke: *Appl. Phys. Lett.*, **86**, 131915 (2005).
13) T. Tanaka, T. Nishiyama, K. Shikada, M. Ohtake, F. Kirino, and M. Futamoto: *J. Magn. Soc. Jpn.*, **34**, 21 (2010).
14) J. Higuchi, M. Ohtake, Y. Sato, T. Nishiyama, and M. Futamoto: *Jpn. J. Appl. Phys.*, **50**, 063001 (2011).
15) G. Wasserman: *Arch. Eisenhüttenwesen*, **16**, 647 (1933).
16) Z. Nishiyama: *Sci. Tohoku Univ.*, **23**, 638 (1934).
17) G. Kurdjumov and G. Sachs: *Z. Phys.*, **64**, 325 (1930).
18) T. Soda, S. Minakawa, M. Ohtake, M. Futamoto, and N. Inaba: *IEEE Trans. Magn.*, **51**, 2000904 (2015).
19) H. Shoji: *Z. Kristallogr.*, **84**, 74 (1932).
20) Z. Nishiyama: *Sci. Rep. Res. Inst. Tohoku Univ. A*, **25**, 76 (1936).

Received Mar. 7, 2015; Accepted May 26, 2016